Mechanically coupling on the plate interface in the Nankai trough, Japan and a possible seismic and aseismic rupture scenario for megathrust earthquakes

Tatsuhiko Saito[1] and Akemi Noda[2]
[1]National Research Institute for Earth Science and Disaster Resilience, Tsukuba, Japan,
[2]Meteorological Research Institute, Tsukuba, Japan

Corresponding author: Tatsuhiko Saito (saito-ta@bosai.go.jp)

Keypoints

- An inversion method for the shear stress rate distribution along a plate boundary is developed.
- Mechanically coupled areas are identified on the plate interface in the Nankai trough.
- A possible scenario for a megathrust earthquake after an afterslip of a foreshock is proposed based on the coupling distribution.

Index terms

8118 Dynamics and mechanics of faulting (Tectonophysics)

7240 Subduction zones (Seismology)

4316 Physical modeling (Natural Hazards)

Abstract

Quantifying the stress distribution or finding mechanically coupled areas on the plate interface is fundamentally important for conjecturing megathrust earthquakes that may occur in the future. Kinematically coupled areas, or slip deficit distributions, on plate interfaces were commonly estimated by geodetic-data analyses. However, mechanically coupled areas are not identical to the kinematically coupled areas. The present study develops an inversion method to estimate the stress rate distribution as mechanically coupled areas. We apply this method to the Nankai trough subduction zone, southwestern Japan to detect mechanically coupled areas. Some of the estimated coupled areas correspond to the rupture areas of historical earthquakes. Others are in a deeper part, which may release the stress as aseismic slip. We then construct a rupture scenario that can occur in the Nankai trough in the future based on the estimated mechanical coupling, assuming that an effective stress accumulation period is 100 years. The scenario consists of a foreshock of M_W 8.0 followed by an afterslip of M_W 7.9 and a mainshock of M_W 8.2. Although the moment magnitude of the afterslip is similar to the foreshock, the energy released by the foreshock is significantly larger than the afterslip because the stress drop of the afterslip is small.

Plain Language Summary

The driving force that generates huge earthquakes originates from the coupling between overriding continental plate and subducting oceanic plate. How strong and which parts are coupled along the plate interface provide us with critical information for megathrust earthquakes that may occur in the future. Significantly coupled areas along the plate interface can be detected by the analysis of ground deformation. However, it is difficult to obtain a correct information about the stress of the coupling. To quantify the coupling along the plate interface, this study develops a method to estimate the stress rate based on elastic mechanics. We apply the method to the Nankai trough, in southwestern Japan, to estimate the plate coupling. Then, by using the estimated coupling information, we create a scenario for a sequence of earthquakes. This consists of a foreshock, a mainshock, and a slow slip between the foreshock and the mainshock. This study provides a method to obtain critical information about the mechanics on the plate boundary based on which we can create megathrust rupture scenarios.

1. Introduction

The coupling between the overriding plate and the subducting plate is one of the most fundamental concepts for the generation of megathrust earthquakes. There are two types of definitions for coupling: kinematic coupling and mechanical coupling. It is important to recognize the difference between the two definitions (Wang and Dixon 2004). The mechanically coupled areas are the places where the shear stress is higher than the surrounding area due to higher friction coefficient or higher effective normal stress. As a result, a slip on the plate interface that is smaller than the average slip over the subducting plate, which we call slip deficit, occurs in and around the region. The slip deficit area is recognized as a kinematically coupled area. Typically, a kinematically coupled area is wider than a mechanically coupled area. In an extreme case, the kinematic coupling can occur even at a place where there is no stress or no friction if the adjacent mechanically coupled area causes the slip deficit (e.g., Herman et al. 2018). In such a case, significant coseismic slip can occur without a local stress drop at the coseismic rupture. Actually, a large slip near the trench in the 2011 Tohoku-Oki earthquake was reported to be excited without a significant local stress drop, but was brought about by the fracture of the deeper part of the mechanically coupled area (Murphy et al. 2018; Lindsey et al. 2021). It is the mechanical coupling that essentially gives a driving force or strain energy to generate earthquakes, and the kinematic coupling is a result of the mechanical coupling.

Kinematically coupled areas have been commonly detected at various subduction zones by geodetic data analyses with the concept of back slip (e.g., Savage 1983). The coupled areas are also used for the assessment of megathrust earthquakes that may occur in the future (e.g., Baranes et al. 2018; Loveless and Meade 2015; Watanabe et al. 2018; Graham et al. 2021). Some studies reported that the slip deficit estimated before the earthquake roughly matched the earthquake rupture area. For example, for the 2009 Chilean earthquake, a portion of the main slip area was detected as the slip deficit before the earthquake (Lorito et al. 2011). Also, for other events, the areas of the coseismic rupture and the slip deficit during the interseismic period were in good agreement (Protti et al. 2014; Hashimoto et al. 2009; 2012; Loveless and Meade 2011). However, kinematical modeling does not always derive reasonable mechanical properties. Analyzing data containing coherent noise without appropriate constraints in inversion will result in a biased slip-deficit distribution causing an unrealistically extreme stress concentration or negative stress accumulation. We should consider not only kinematic coupling but also mechanical coupling to obtain a reliable model for the plate coupling.

There have been fewer studies that estimated the distributions of mechanically coupled areas. Herman and Govers (2020) proposed an inversion analysis to determine the locked areas and found that less than 30 % of the total plate boundary is mechanically coupled along the South America subduction zone. Other studies estimate the mechanically coupled areas from the results of the slip deficit rate distributions based on continuum mechanics (e.g., Hok et al. 2011; Noda et al. 2018). Smoothing constraints are introduced in the kinematic inversions to avoid an unnecessarily large stress rate. Lindsey et al. (2021) developed a method to estimate the slip deficit distribution with an appropriate constraint for the shear stress rate distribution along the plate interface. Once we obtain the distributions of the mechanically coupled areas along the plate boundary, we can simulate possible earthquake ruptures by directly using them for the stress drop parameters based on earthquake mechanics (Hok et al. 2011; Yang et al. 2019; Noda et al. 2021).

The present study proposes a method to estimate shear-stress rate distributions and applies it to identify mechanically coupled areas along the Nankai Trough subduction zone,

southwestern Japan. Moreover, based on the shear stress distribution reconstructed from the estimated mechanically coupled areas assuming a stress-accumulation time, we create a possible earthquake sequence that could occur in the future. Section 2 explains the tectonic setting and a plate interface model in the Nankai trough used in this study. Section 3 develops an inversion method for stress rate distribution at the plate interface. In Section 4, we apply the method to the geodetic data detected by onshore and offshore GNSS stations at the Nankai trough. In Section 5, we show an example for a possible earthquake sequence scenario where a megathrust mainshock follows an afterslip of a foreshock from the estimated mechanically coupled areas. Section 6 discusses the estimated mechanically coupled areas and the energetics of the earthquake sequence. Section 7 concludes this study.

2. Nankai Trough Subduction Zone

2.1 Megathrust earthquakes

In southwestern Japan, the Philippine Sea plate subducts under the Amurian plate at a horizontal velocity of ~6 cm/year (DeMets et al. 2010) (Figure 1). Huge interplate earthquakes repeatedly occurred with the order of a recurrence interval of about 100 years (e.g., Ando 1975; Ishibashi and Satake 1998; Seno 2012). The rupture areas of the historical earthquakes were composed of various combinations of segmented areas. Five segments A, B, C, D, and E are proposed as shown in Figure 1 (Ishibashi and Satake 1998). The last earthquake sequence was the 1944 Tonankai earthquake (M 7.9) with the rupture areas of C and D and the 1946 Nankai earthquake (M 8.0) with the rupture areas of A and B. The 1707 Hoei earthquake (M 8.6) has been considered to have ruptured all areas (A, B, C, D, and E). Since seismograms are not available for historical events prior to the nineteenth century, there is some discussion about a possible rupture area for the 1707 Hoei earthquake. Recently, Furumura et al. (2011) proposed that the western edge of the segment A should be extended farther west. Seno (2012) remarked that segment E did not rupture at the 1707 Hoei earthquake.

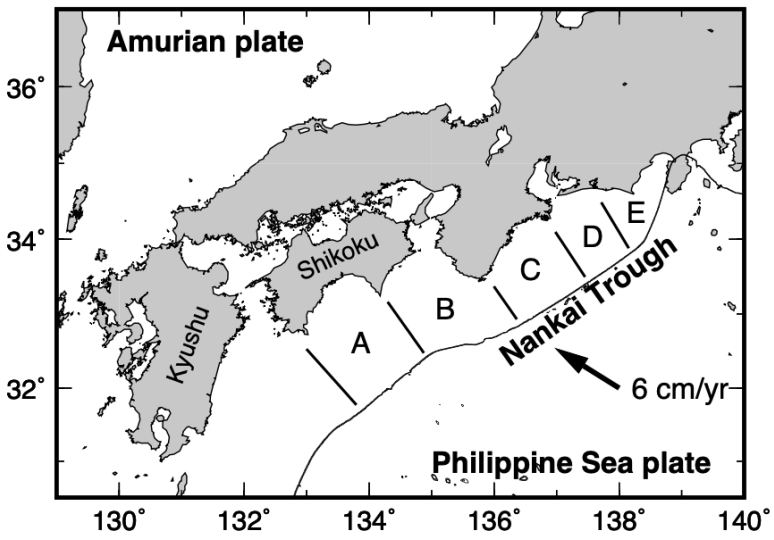

Figure 1. Tectonic setting and segmentation structure of the Nankai Trough, Japan. The Philippine Sea plate subducts under the Amurian plate at a horizontal velocity of ~6cm/year. Rupture areas of historical earthquakes are composed of different combinations of the segmented areas.

2.2. Plate interface model

We use the plate interface model in a 3-D subsurface velocity structure model referred to as the Japan Integrated Velocity Structure Model (JIVSM). The JIVSM was constructed from hypocenter distributions and subsurface exploration analyses (Koketsu et al. 2012). This model is used in various studies such as seismic wave propagation simulations (e.g., Maeda et al. 2017) and kinematic earthquake source process or CMT solution analyses in the 3-D structure (e.g., Takemura et al. 2020). The plate interface is given by the depth from the sea surface. The 5.25 km depth contour agrees with the contour of the deepest sea depth (a bold gray dashed line in Figure 2a). Since a kink of the rupture surface causes unreasonably large stress concentration in elastic medium (e.g., Romanet et al. 2020), we apply a spatial low-wavelength pass filter to the plate interface to remove short-wavelength heterogeneity (Supporting information Text S1). We set the sea surface at z = 0 km and set a flat sea bottom at z = 5.25 km as a traction-free surface. We will calculate the displacements at the free surface in an elastic half-space to compare the observed displacements on the sea bottom and on the ground surface. We represent the plate interface with 5383 triangular elements with side lengths of approximately 10 km (Figure 2a). This study uses the Cartesian coordinate where the x-axis is taken as north, the y-axis as east, and the z-axis as vertically downward (Aki and Richards 2002).

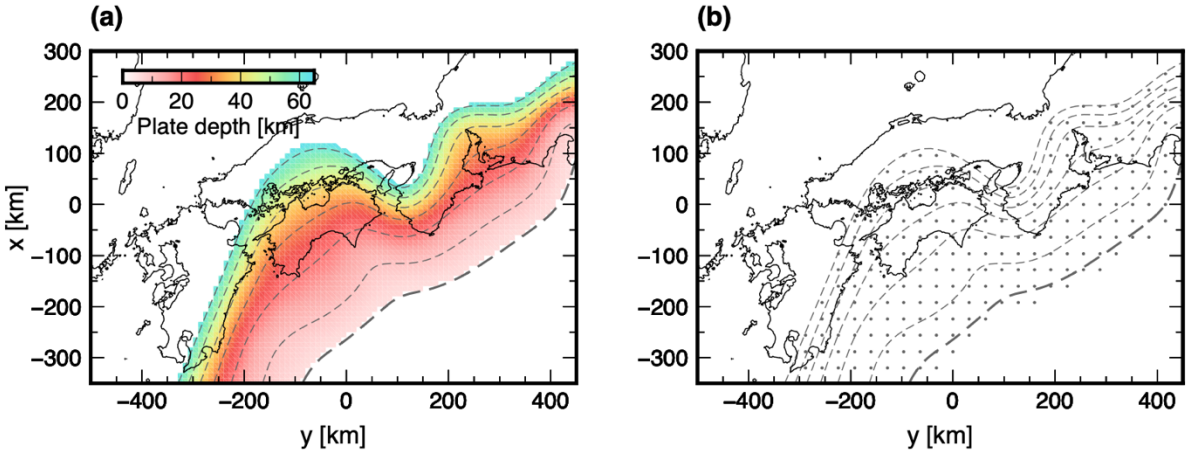

Figure 2. (a) The plate interface of the subducting Philippine Sea plate. The depth of the interface measured from the sea surface is contoured at a depth of 5.25 km with the bold gray dashed line and 10, 20, 30, 40, 50, and 60 km with the fine dashed lines. The trench corresponds to a depth of 5.25 km of the plate interface. We set a flat sea bottom at z = 5.25 km as a traction-free surface. (b) The locations of the center of the 256 basis functions are plotted by dots.

3. An Inversion Method for Mechanical Coupling Distribution

3.1. Displacement velocity and stress velocity

This section explains a method for estimating the stress rate along the plate interface. We take a unit vector in the slip direction $\mathbf{e}_{\mathrm{slip}}(\mathbf{x})$ that is in the same direction as the movement of the Amurian plate (hanging wall) with respect to the Philippine Sea plate (foot wall). Then, the slip direction points to the southeast (approximately N120°E). The 3-D slip vector is estimated from the plate motion vector in MORVEL (DeMets et al. 2010) and the plate interface geometry. The slip vector is then given by $\mathbf{s}(\mathbf{x},t) = s(\mathbf{x},t)\mathbf{e}_{\mathrm{slip}}(\mathbf{x})$. When the slip amount $s(\mathbf{x},t)$ is negative, it represents the slip deficit along the plate interface. The traction on the plate interface caused by the slip distribution is denoted by $\mathbf{t}(\mathbf{x},t)$. Assuming that the shear stress dominates in the slip direction, we give the shear stress as the inner product of the traction and the slip direction as $t_s(\mathbf{x},t) = \mathbf{t}(\mathbf{x},t)\cdot\mathbf{e}_{\mathrm{slip}}(\mathbf{x})$. The positive shear stress represents mechanical coupling between the overriding and subducting plates. We will estimate the rate of the shear stress $\dot{t}_{\mathrm{s}}(\mathbf{x},t)$ from GNSS displacement rate data.

We represent the shear stress rate distribution $\dot{t}_{\mathrm{s}}(\mathbf{x},t)$ as the sum of the Gaussian-type basis functions. The j-th basis function $f^j(\mathbf{x})$ of which center is located at (x_j, y_j, z_j) on the plate interface is given by

$$f^j(\mathbf{x}) = e^{-\frac{(x-x_j)^2+(y-y_j)^2}{a^2}}. \tag{1}$$

The shear stress rate distribution is given by

$$\dot{t}_{\mathrm{s}}(\mathbf{x},t) = \sum_{j=1}^{M} m_j(t) f^j(\mathbf{x}) = \sum_{j=1}^{M} m_j(t) e^{-\frac{(x-x_j)^2+(y-y_j)^2}{a^2}} \tag{2}$$

where the coefficient m_j has a dimension of stress rate (e.g., MPa/year) and the spatial size of each basis function is set as $a = 32$ km. We set the total number of the basis functions as $M = 256$. Figure 2b shows the locations of (x_j, y_j) $(j = 1,2,\cdots 256)$ for each basis function. The grid spacing is set as 32 km in the (x, y) coordinates.

We then obtain the slip distribution $g^j(\mathbf{x})$ generating the stress change represented by the j-th basis function of $f^j(\mathbf{x})$ in an elastic half-space medium. To obtain $g^j(\mathbf{x})$, we calculate the stress change at the center of the kth triangular element caused by unit slip at the lth triangular element $G_{kl}^{traction}$ where $k, l = 1,\cdots, N$ (N=5383) by using an algorithm of Nikkhoo and Walter (2015). The $G_{kl}^{traction}$ has a dimension of stress over slip (e.g., MPa/m). By using the matrix $G_{kl}^{traction}$, we can represent the non-dimensional stress distribution $f^j(\mathbf{x})$ (Eq. (1)) caused by the slip distribution $g^j(\mathbf{x})$ as

$$f^j(\mathbf{x_k}) = \sum_{l=1}^{N} G_{kl}^{traction} g^j(\mathbf{x_l}) \quad (k = 1, \ldots, N) \tag{3}$$

where the slip distribution $g^j(\mathbf{x})$ has a dimension of slip over stress (e.g., m/MPa). By solving the system of equations of Eq. (3), we estimated the slip distribution $g^j(\mathbf{x_l})$ that excites the j-th stress change $f^j(\mathbf{x_k})$ $(k = 1,\cdots, N)$. For example, Figures 3a and 3b show the j-th $(j = 105)$ stress change distribution $f^{105}(\mathbf{x})$ and the corresponding slip distribution $g^{105}(\mathbf{x})$. The stress

change distribution $f^j(\mathbf{x})$ shows a concentric pattern given by Eq. (1) (Figure 3a). On the other hand, for the slip distribution $g^j(\mathbf{x})$ the slip is amplified near the free surface and the concentric pattern is distorted (Figure 3b). This indicates that the slip deficit can occur even in a region without mechanical coupling.

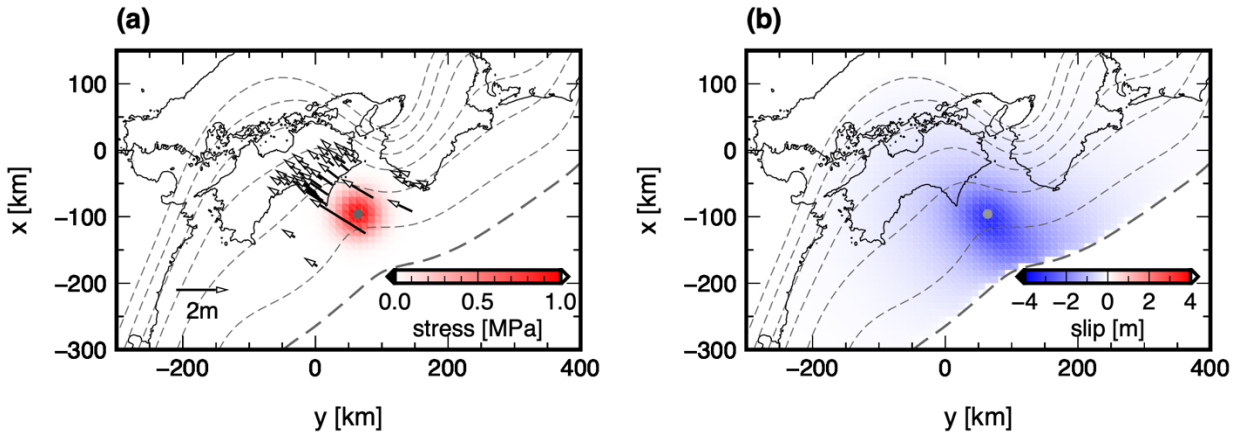

Figure 3. (a) An example of the basis function of the stress change distribution f^j given by Eq. (1) where $j = 105$ and the location of the center is given by a small gray circle ($y_{105} = 64$ km East, and $x_{105} = -96$ km North). The dimension of MPa is multiplied by the stress change distribution for intuitive understanding of the response. The horizontal displacements $\mathbf{h}^{105}$ caused by the stress-rate basis function f^{105} are plotted by arrows. (b) The distribution of the slip g^j that causes the stress change distribution in (a).

We then calculate the horizontal velocity vector $\mathbf{h}^j(x, y)$ on the free surface. This is calculated from the slip distribution $g^j(\mathbf{x})$ in an elastic half-space (Nikkhoo and Walter 2015). This horizontal vector has a dimension of displacement per stress (e.g., m/MPa). We show the horizontal displacement $\mathbf{h}^{105}(x, y)$ in Figure 3a as an example.

As a result, when the stress rate distribution is given by Eq. (2) using the coefficients m^j for the jth basis function, the slip velocity $\dot{\mathbf{s}}(\mathbf{x}, t)$ at the plate interface is given by

$$\dot{\mathbf{s}}(\mathbf{x}, t) = \sum_{j=1}^{M} g^j(\mathbf{x})\, m^j(t) \tag{4}$$

and the horizontal velocity at the surface is given by

$$\dot{\mathbf{u}}(x, y, t) = \sum_{j=1}^{M} \mathbf{h}^j(x, y)\, m^j(t). \tag{5}$$

where M is the number of the basis functions ($M = 256$).

3.2 Inversion Analysis

We can estimate the stress rate on the plate interface from the surface velocity using Eq. (5). However, the actual surface velocity observed at GNSS stations includes the deformation from block motions and inelastic deformations inside the overriding continental plate in addition to the deformation caused by the slip along the plate boundary (e.g., Nishimura et al. 2018; Noda et al. 2018). Since such deformations are not explained by the assumed model, they behave as coherent noise and will bias the result. To minimize the contributions from the sources in the continental plate, we use the surface strain as data in the inversion analysis (e.g., Noda, A. et al. 2013). We construct triangular meshes consisting of the GNSS observation points based on Delaunay triangulation. We then estimate the horizontal strain rate $\dot{\boldsymbol{\epsilon}} = (\dot{\epsilon}_{xx}, \dot{\epsilon}_{xy}, \dot{\epsilon}_{yy})$ at each cell from observed velocity $\dot{u}_x$ and $\dot{u}_y$ at each GNSS station assuming the strain rate in each triangular element is constant. Then, based on Eq. (5), we use the linear relation

$$\dot{\boldsymbol{\epsilon}}^i = \sum_{j=1}^{M} \mathbf{G}_{ij}^{\epsilon}\, m^j. \tag{6}$$

to estimate m^j from the observed strain rate at the ith point. The matrix $\mathbf{G}_{ij}^{\epsilon}$ represents the strain rate at the ith point caused by the jth basis function of the stress rate at the plate boundary. Here, we assume that the strain rate $\dot{\boldsymbol{\epsilon}}^i$ and the stress rate coefficient m^j do not change over time.

4. Data Analysis

4.1 Data

We use GNSS horizontal displacement rates obtained from daily coordinate data of GEONET (Sagiya, 2004) from March 2005 to February 2011 by the same procedure in Noda et al. (2018). We also use seafloor geodetic data obtained from GNSS-Acoustic observations from 2006 to 2015 (Yokota et al. 2016). We don't use any weighting functions in our inversion analysis for land and seafloor data sets. Figure 4 shows the horizontal velocity used for the inversion analysis in this study. The southern coast side is moved northwest due to the subducting Philippine Sea plate with a velocity of about ~50mm/yr.

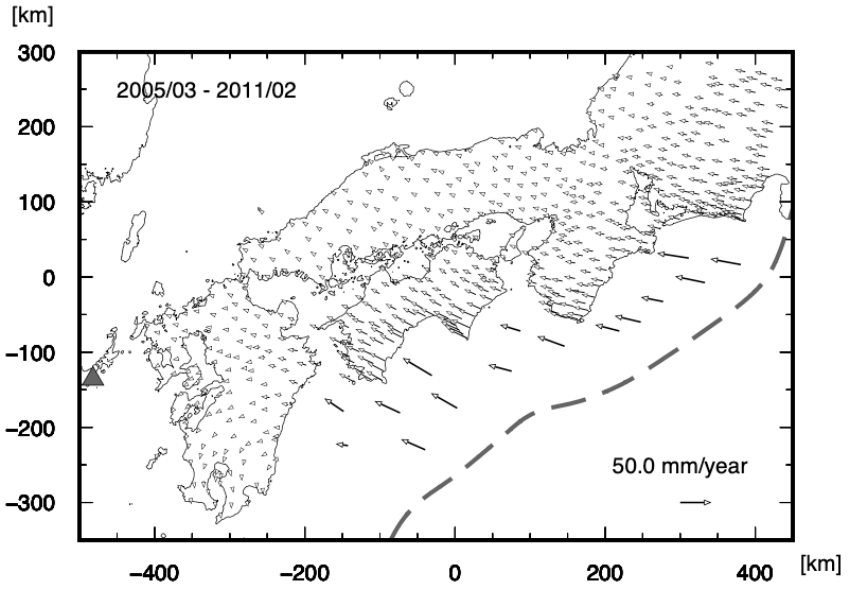

Figure 4. Horizontal velocities obtained from GNSS from March 2005 to February 2011and GNSS-Acoustic observations (Yokota et al. 2016) in southwestern Japan. The relative velocity vectors at the GNSS stations to the reference point Fukue station (a gray triangle) and the seafloor velocities with respect to the Amur plate are plotted.

We calculate the strain rate at 1114 triangular elements from the horizontal displacements. Figures 5a-c shows each component of the strain rate tensor at each point. On the Shikoku island ($x = \sim -50$ km, $y = \sim -80$km), the dominant deformation shows NS and EW contraction and shear deformation of the order of ~0.1 mm/km/year = 10^{-7}/year.

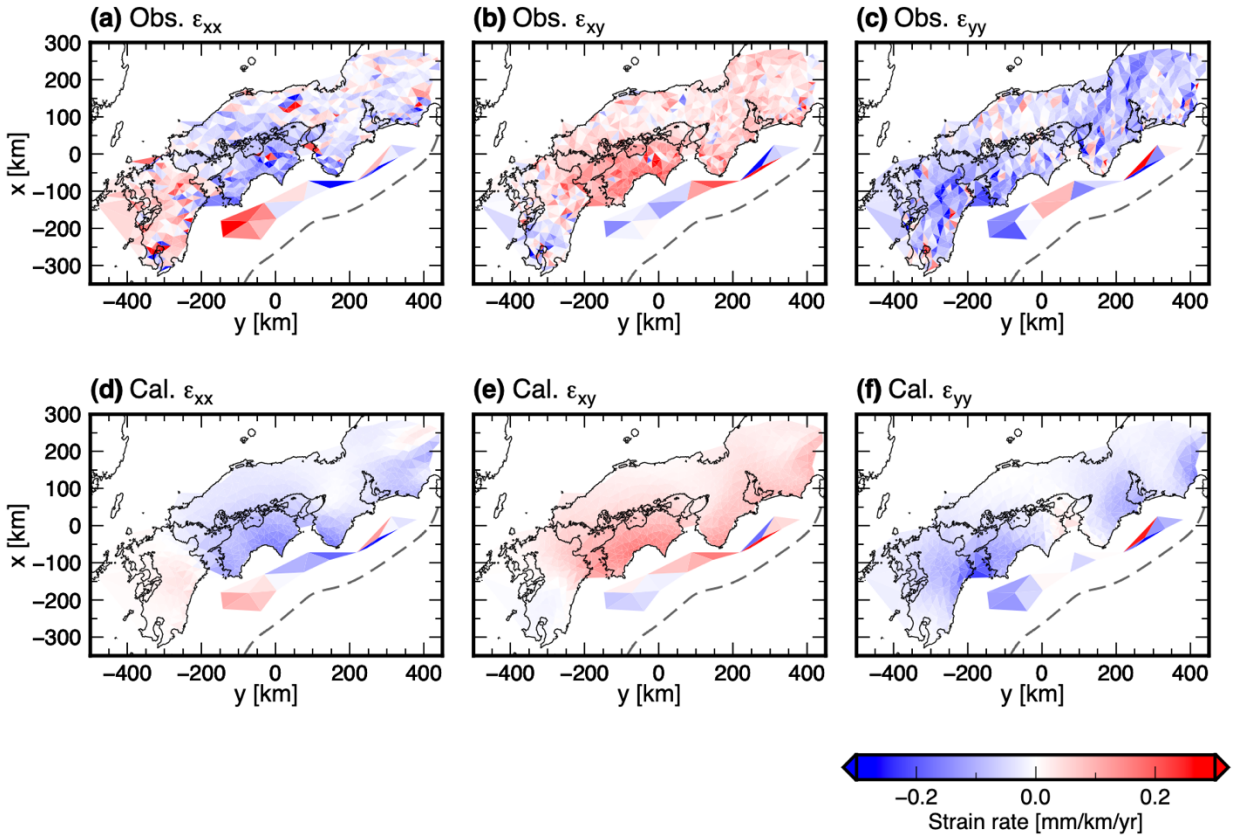

Figure 5. The horizontal strain rates transformed from GNSS velocity data: (a) ϵ_{xx}, (b) ϵ_{xy}, and (c) ϵ_{yy} (x: north and y: east). The corresponding strain rates calculated from the estimated plate coupling: (d) ϵ_{xx}, (e) ϵ_{xy}, and (f) ϵ_{yy}.

We suppose that the stress rate is basically positive along most of the plate interface during the interseismic period (e.g., Lindsey et al. 2021) and estimate m^j with a non-negative, damping inversion scheme. We minimize the value

$$\sum_{i=1}^{N_d} \left| \dot{\epsilon}^i - \sum_{j=1}^{M} G_{ij}^{\epsilon}\, m^j \right|^2 + \alpha^2 \sum_{j=1}^{M} \left| m^j \right|^2 \tag{7}$$

under the constraint $m^j > 0$ to estimate m^j. The total number of data is $N_d = 1114 \times 3$. We set $\alpha = 0.02$ [m/km/MPa] by trial-and-error to obtain a stable stress rate distribution.

4.2. Results

The estimated stress rate distribution is shown in Figure 6a. The surface strain rates calculated from the estimated stress rate are compared in Figures 5d, 5e, and 5f, which nicely reproduces the long-wavelength components of the strain rate distribution. In Figure 6a indicates that high-shear-stress-rate regions marked as Muroto, Kii, Kumano, and Enshu are on the plate interface shallower than 25 km. The place marked as Bungo is on the deeper plate interface around 30 km depth. In these areas, the shear stress is accumulated at > ~2kPa/year. If the stress

accumulates for ~100 years, these areas are expected to host earthquakes with a stress drop of > ~0.2MPa. These high-stress-rate distributions (Bungo, Mouroto, Kii, Kumano, and Enshu) are similar to the stress rate distribution estimated from the slip deficit rate distribution in Noda et al. (2018; 2021). The high-stress regions of Muroto, Kii, Kumano, and Enshu may persist for a long time and caused historical Nankai trough earthquakes (e.g., Baba et al. 2002; Murotani et al. 2015; Sagiya and Thatcher 1999; Tanioka et al. 2001).

Figure 6b shows a slip deficit rate distribution (derived using Eq. (4)) indicating that there are dominant slip deficit rates (> 6cm/year) at Muroto and Kii. Also, we recognize that the high-slip-deficit areas look smoother than the stress-rate distributions. These slip-deficit distributions are similar to those in previous studies (e.g., Noda et al. 2018; Hori et al. 2021). This supports the validity of the method proposed in this study.

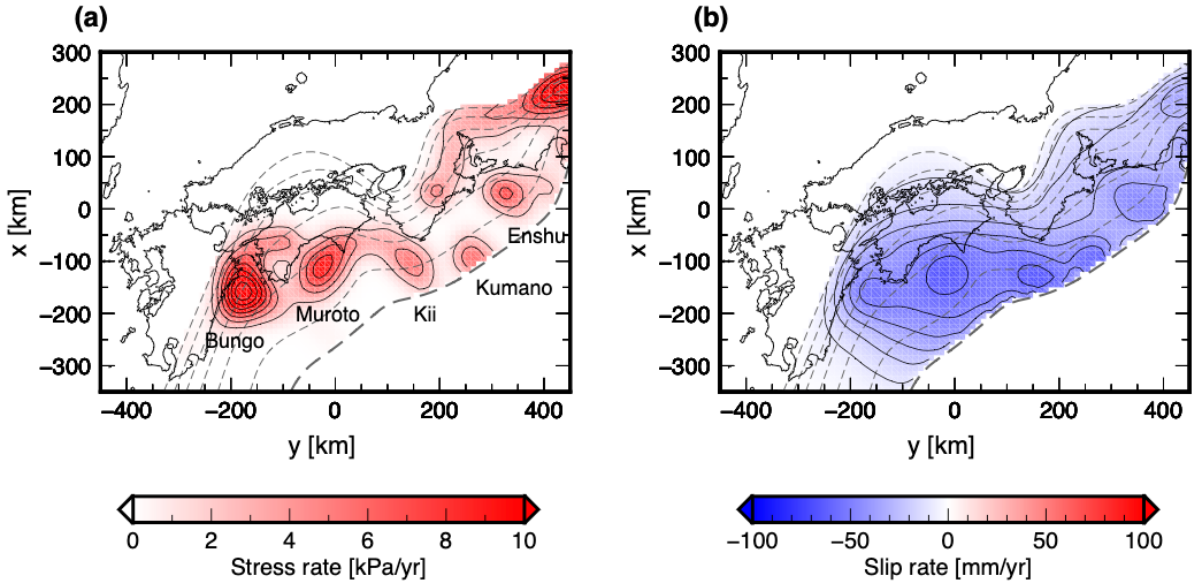

Figure 6. (a) Estimated shear stress rate at the plate interface. Contour lines are plotted at 2kPa/year intervals. (b) Slip deficit rate at the plate interface. Contour lines are plotted at 10mm/year intervals.

4.3 A recovery test of stress distribution

To check the resolution of the stress rate distribution estimation, we perform a recovery test. We suppose a stress rate distribution as shown in Figure 7a which is a simplified distribution for the estimated stress distribution. We then added random noise with a standard deviation of 8×10^{-8} [1/year] obtained by comparing the strain rate data we used in the inversion and the theoretical strain rates calculated from Figure 6a. We invert the synthesized strain data to recover the stress distribution with the same procedure as in Figure 6. We also set the same value of α as Figure 6. Figure 7b shows the result indicating that the overall pattern of five highly stressed regions was recovered. The recovered distribution is smoother than the targets. In particular, the highly stressed areas of Kii and Kumano show relatively lower resolution. We should note that the low-frequency earthquakes and long-term slow slip event occurred near the trench around Kumano (e.g., Obara and Kato 2016). On the other hand, the Kumano area in Figure 6 corresponds to the rupture area of the 1944 Tonankai earthquake (M

7.9) (e.g. Ichinose et al. 2003; Baba and Cummins 2005; Sherril and Johnson 2021). However, based on the result of the recovery test, we might not have clearly resolved the location of the highly stressed area around Kumano. It is possible that the highly stressed area is located slightly landward to avoid the slow earthquake area near the trench. To resolve more precise locations of the highly stressed areas, particularly near the trench, more geodetic observations are needed for offshore regions (e.g.,Yokota et al. 2016; Kimura et al. 2019).

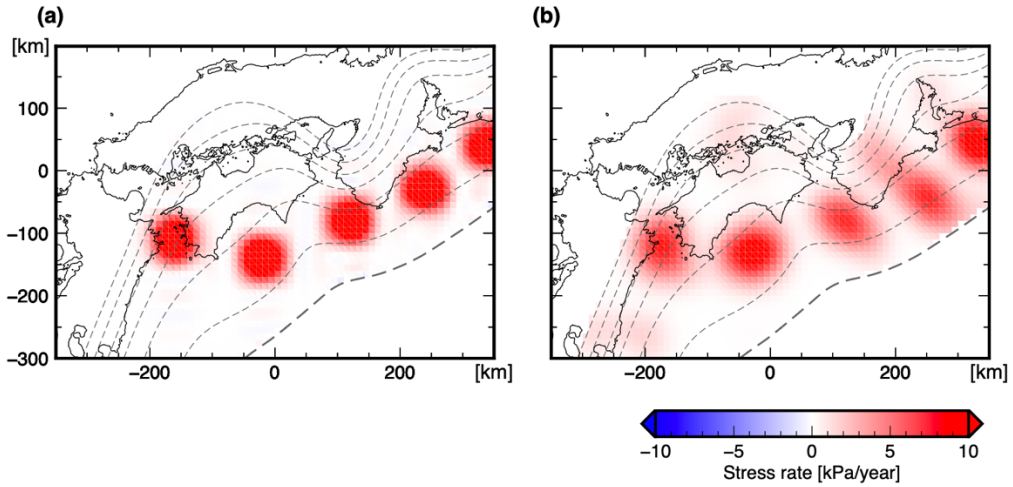

Figure 7. Recovery test for stress rate distribution. (a) Assumed stress distribution. (b) Estimated stress distribution.

5. Possible Rupture Scenario: Seismic and Aseismic Ruptures

Since we have obtained the mechanically coupled distributions, we are able to create rupture scenarios for the Nankai trough earthquakes that may occur in the future. Although the estimated distribution contains uncertainties that will be improved if more offshore observation data are available, the scenario created herein can provide material for further development. This section presents an example about how to construct this scenario.

In the Nankai trough, earthquakes of approximately M 8 – 8.5 occurred successively with different time intervals. The 1854 Nankai earthquake (M 8.4) occurred 32 hours after the 1854 Tonankai earthquake (M 8.4). The 1944 Tonankai earthquake (M 7.9) was followed by the 1946 Nankai earthquake (M 8.0) approximately two years later. The modeling of successive great earthquakes in this region was conducted with earthquake cycle simulations, where the friction distribution was simplified and assumed (e.g., Hori et al., 2004). In subduction zones in the world, large earthquakes can be triggered by a preceding aseismic slip (e.g., Miyazaki et al. 2011; Kato et al. 2012; Ruiz et al. 2014). Hence, in the Nankai trough, the afterslip of a foreshock might cause frictional weakening in neighboring mechanically coupled areas and trigger a larger mainshock earthquake. In other words, the afterslip of the foreshock might work as a pre-slip for a mainshock. Therefore, we consider a possible scenario including a foreshock, an aseismic slip, and a mainshock.

Assuming that earthquakes are generated by the stress, particularly, the amount of stress that has been accumulated since the previous earthquake, we assume that the stress accumulated over a certain period is the stress drop for coseismic ruptures (e.g., Hok et al. 2011). We also assume that the stress rate of the interseismic period is constant and the stress accumulation time is 100 years. Note that the stress rate can change during the interseismic period by viscoelastic

deformation after the previous earthquake (e.g., Sasajima et al. 2019; Li et al. 2020). Hence, we should consider the accumulation time of 100 years here as an effective accumulation time rather than the actual time. Figure 8 shows the accumulated stress on the plate interface when we set the effective accumulation time at 100 years. Stresses are accumulated significantly in areas labeled Mu, Ki, Ku, and En at depths shallower than approximately 25 km. At the area labeled by Bu, the depth is rather deep (approximately 30 km) where slow slip events (M_W 6.8-6.9) repeatedly occurred at an interval of approximately six years (Hirose et al. 2005; Takagi et al. 2016). We hence consider that the stress may be released aseismically in the Bu region.

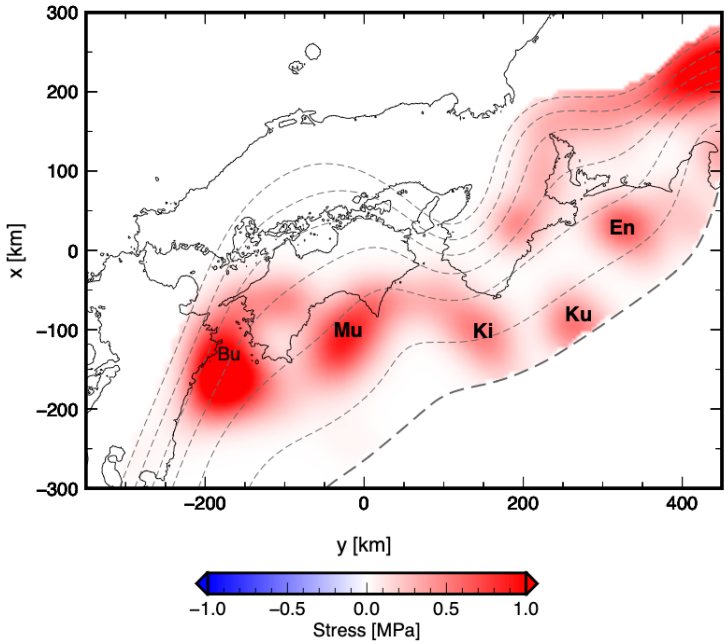

Figure 8. Stress accumulation for 100 years, where the estimated stress rate distribution does not change with time.

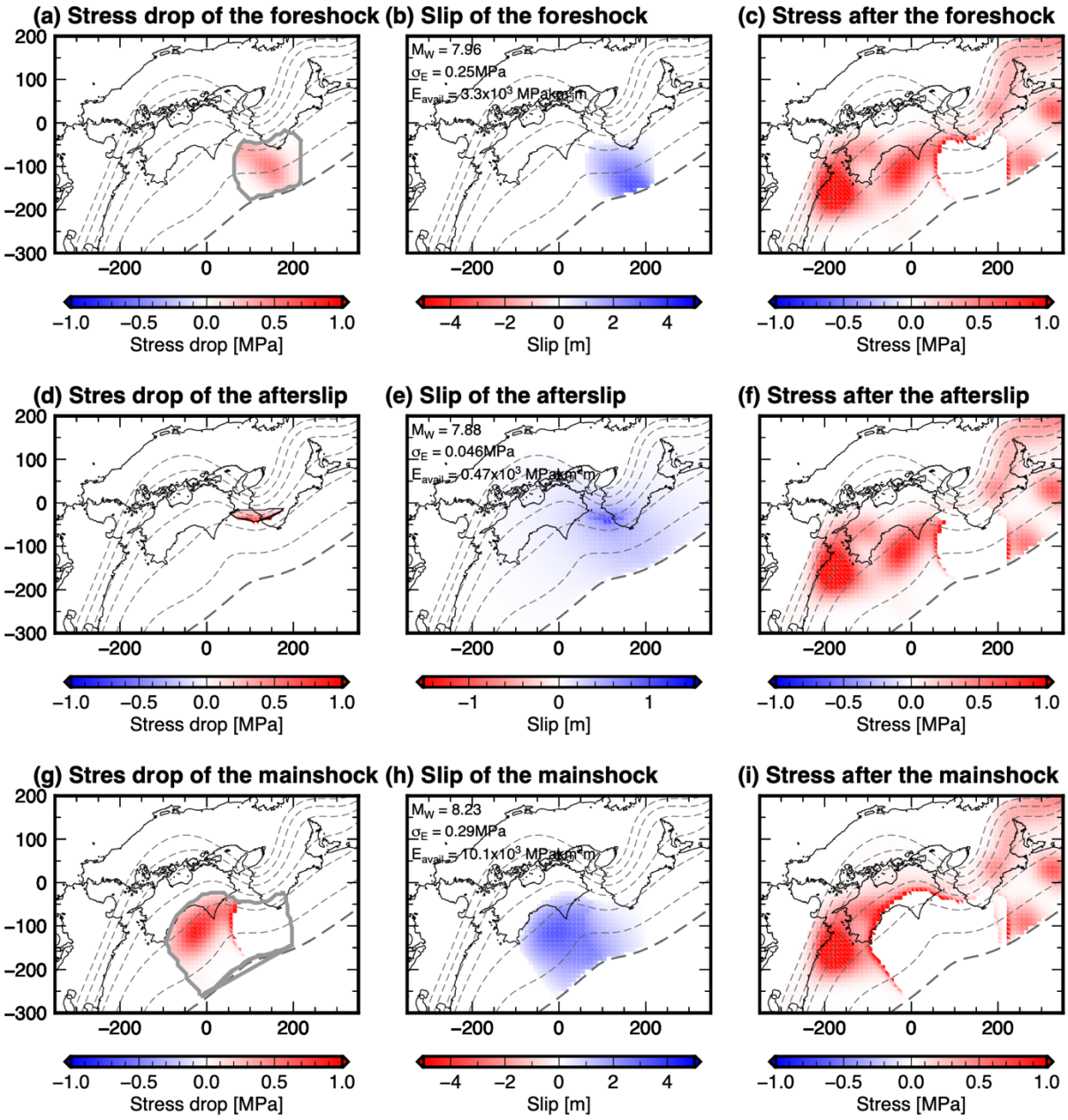

Figure 9. Possible rupture scenario including a foreshock, an afterslip, and a mainshock created based on the stress accumulated for 100 years. (a) Stress drop of the foreshock. The gray line indicates the rupture area where we set the stress drop and slip is allowed. Slip is not allowed outside the rupture area. (b) Slip distribution of the foreshock. (c) Stress distribution after the foreshock. (d) Stress drop of the afterslip. The black line indicates the area where we set the stress drop. Slip is allowed on the whole plate interface. (e) Slip distribution of the afterslip. The range of the color bar is different from those in (b) and (h). (f) Stress distribution after the afterslip. (g) Stress drop of the mainshock. The gray line indicates the rupture area (h) Slip distribution of the mainshock. (i) Stress distribution after the mainshock.

In Figure 8, we assume that a foreshock occurs as the strain energy release by the fracture of mechanically coupling area Ki. Assuming that seismic slip occurs at a depth shallower than 25 km, we selected the foreshock rupture area as indicated by the gray line in Figure 9a and calculated the slip distribution of the foreshock. To estimate the slip distribution $g(\mathbf{x})$, we used the following equation:

$$f(\mathbf{x_k}) = \sum_{l=1}^{N_f} G_{kl}^{traction} g(\mathbf{x_l}) \ (k = 1, .., N_f) \tag{8}$$

where $f(\mathbf{x_k})$ is the stress drop distribution for the foreshock (Figure 9a) and $G_{kl}^{traction}$ is the shear stress response that is also used in Eq. (3). We limit the range N_f inside the rupture area ($N_f = 392$). Figure 9b shows the estimated slip distribution of the foreshock. The moment magnitude of this event is M_W 7.96. We calculate the stress distribution after the foreshock by adding the stress change caused by the foreshock to the stress distribution before the foreshock. Figure 9c shows the stress distribution after the foreshock. The stress was increased outside the rupture area.

We suppose that an afterslip follows the foreshock. The stress drop for the afterslip is set at the deeper part of the foreshock as shown in Figure 9d. The aseismic slip area possibly develops with increasing time (Kato et al. 2012; Ruiz et al. 2014). Supposing that the time elapses sufficiently from the foreshock, we did not limit the slip area for the afterslip in our scenario. We used Eq. (8) with all elements $N_f = N(= 5383)$. Here, we assume that the stress drop is zero $f(\mathbf{x_k}) = 0$ outside the area where the stress drop occurs (black line in Figure9d). Figure 9e shows the estimated afterslip slip distribution. The moment magnitude is M_W 7.88, which is similar to the foreshock. The stress distribution after the afterslip is shown in Figure 9f.

We then suppose that the afterslip that invades in the high-stress region of Muroto (marked as Mu) triggers a mainshock. Assuming that the rupture area of the mainshock is located in the shallower part (depth: < 25km), we set the rupture area for the mainshock (Figure 9g). As in the case of the foreshock, we estimated the slip distribution based on Eq. (8) ($N_f = 910$) from the stress drop. Figure 9h shows the slip distribution of the mainshock. The moment magnitude was M_W 8.23, which is significantly greater than the foreshock and the aftershock. While the higher stress area is located at a depth of between 10 and 20 km and does not reach the free surface (Figures 9f and 9g), significant slip occurs near the trench due to the effects of the free surface (Figure 9h).

6. Discussion

6.1 Energetic consideration

We showed a rupture scenario of a foreshock (M_W 7.96), an afterslip (M_W 7.88), and the main shock (M_W 8.23). The moment magnitude of the afterslip was almost the same as that of the foreshock. Here we examine these events from the viewpoint of energy. The elastic strain energy released from the lithosphere by an earthquake is one of the most fundamental quantities that characterize the earthquake (e.g., Kostrov 1974). However, the released strain energy depends on the initial stress, which is uncertain in the lithosphere. To avoid this difficulty, Kanamori (1977) assumed a complete stress drop for an earthquake and used

$$W_0 = \frac{1}{2}\iint_{\Sigma} D_i \left(T_i^{\mathrm{ini}} - T_i^{\mathrm{fin}}\right) dS \tag{9}$$

as a measure of a strain energy related to the earthquake faulting. This is often called the minimum strain energy or the available energy. Using the energetic stress drop $\Delta\sigma^E$ (Noda, H. et al. 2013):

$$\Delta\sigma^E = \frac{\mu}{M_0}\iint_{\Sigma} D_i \left(T_i^{\mathrm{ini}} - T_i^{\mathrm{fin}}\right) dS, \tag{10}$$

the minimum strain energy is represented as

$$\Delta W_0 = \frac{1}{2\mu} M_0 \Delta\sigma^E. \tag{11}$$

The energetic stress drop $\Delta\sigma^E$ becomes greater when the slip or stress has more short-wavelength components (Noda, H. et al. 2013; Saito and Noda 2020). Hence, the energetic stress drop and the minimum strain energy of our rupture scenario constructed from the stress distribution estimated from a GNSS data inversion are basically smaller than actual values because our rupture scenario may lack the short-wavelength components.

The estimated energy W_0 of the foreshock, the afterslip, and the mainshock were 3.3×10^{15}J, 0.47×10^{15} J, and 10.1×10^{15} J, respectively. Although the seismic moments of the foreshock and the aftershock were almost the same, the minimum strain energy of the foreshock was about seven times larger than that of the afterslip. This is because the stress drop of the afterslip is substantially smaller than the foreshock. The minimum strain energy in addition to the seismic moment would be important to characterize the size or magnitude of earthquake faulting when considering earthquake mechanics.

6.2 Afterslip scenarios

Mainshock rupture scenarios were proposed in some previous studies and the scenarios were often used for hazard assessment of strong ground motions and tsunamis (e.g., Hok et al. 2011; Melgar et al. 2016; Yang et al. 2019). On the other hand, few studies include afterslip scenarios. However, monitoring afterslips is very important for the assessment of megathrust rupture occurrence because the afterslip or aseismic slips possibly trigger larger earthquakes (e.g., Matsuzawa et al. 2010; Segall and Bradley 2012). In order to create useful sequential rupture scenarios, it is necessary to understand more deeply the relation between aseismic slip and main ruptures and include possible aseismic slips in the rupture scenarios. There are at least two different driving forces causing afterslips: (i) the stress that the mainshock loads on the surroundings and (ii) the stress that is stored during the interseismic period. For example, in the case of the 2011 Tohoku earthquake, the afterslip that occurred around the mainshock large slip area may be caused by the stress loaded by the mainshock (Agata et al. 2019; Fukuda and Johnson 2021). On the other hand, the afterslip also occurred off Fukushima, which is approximately 200 km away from the epicenter (e.g., Iinuma et al. 2016), where no large significant stress change was expected from the mainshock. The cause of this afterslip may be the stress accumulated during the interseismic period and the mainshock may serve as a trigger for the afterslip. In order to understand the mechanism of afterslip generation more deeply, it may be useful to quantify the energy balance for the afterslip faulting: strain energy increase by a mainshock, tectonic loading during the interseismic period, and the energy release by the afterslip. As this study showed, quantifying the stress accumulation and the fault motion causing

the strain energy release will work as a basic framework for understanding afterslip mechanics. Hence, it would be important to measure not only the seismic moment but also the minimum strain energy or the distribution of the stress change on the afterslip fault surface. It will be necessary in future studies to deepen our knowledge about afterslip or aseismic slip generation associated with large earthquakes to create more realistic and useful rupture scenarios for a sequence of earthquake ruptures.

6.3 Plate interface and subsurface structure

Some studies estimating slip deficit distributions used a plate interface model that is different from that used in earthquake hypocenter determination. This difference sometimes causes a difficulty in a detailed comparison between the plate-coupling distributions and hypocenter distributions. This study used a plate boundary model, the JIVSM (Koketsu et al. 2012), which is also used for 3-D seismic wave propagation and earthquake and slow earthquake hypocenter distributions around the Nankai trough (e.g., Maeda et al. 2017; Takemura et al. 2020). The common plate interface model between seismic and geodetic data analyses enables us to compare the coupling distributions with the coseismic slips, aseismic slips, and aftershock distributions in detail on the same plate interface. This would be useful to monitor seismic and aseismic activities and estimate the change of the mechanical state, such as the stress and friction properties on the plate interface associated with large earthquakes and aseismic slips.

This study assumed a homogeneous half-space elastic medium to calculate the deformation and the stress. The viscoelastic mantle should be taken into consideration in the future. Noda et al. (2018) showed that the estimated slip deficit distributions can change according to the thickness of the elastic layer overlying the viscoelastic half-space, whereas it was difficult to determine the thickness from the available geodetic data set. Sherrill et al. (2021) analyzed the long-term surface deformation over 70 years assuming a 2-D elastic-viscoelastic structure in the 3-D space. Hori et al (2021) showed that the 3-D elastic structure affects the estimation of the slip deficit distributions in the Nankai trough. The results of the stress estimation can vary according to 3-D subsurface structures. In future, a systematic analysis about the effects of medium heterogeneity on the stress distribution in the Nankai trough is important and the data analysis in the heterogeneous structure will give us a more realistic estimation. At that time, the results in a homogeneous half-space elastic medium in this study will work as a reference for further development.

7. Conclusions

We developed an inversion method to estimate mechanically coupled areas on the plate interface and applied it to the GNSS data observed in southwestern Japan. We found some mechanically coupled areas where the stress rate is greater than 4kPa/yr along the Nankai trough (Figure 6a). Some of them correspond to the rupture areas of the historical Nankai earthquakes. Others found in deeper parts may work as aseismic slips to release stress. Based on the estimated coupled areas, we constructed a rupture scenario that could occur in the future. By assuming the stress accumulation period was 100 years, we obtained the stress distribution on the plate boundary. Earthquake ruptures are supposed to be generated as a result of the stress drop. The scenario we constructed consisted of a foreshock of Mw 8.0 followed by an afterslip of Mw 7.9 and a mainshock of Mw 8.2. Although the moment magnitude of the hypothesized afterslip is more or less the same as the hypothesized foreshock, the energy released by the foreshock is significantly larger than the afterslip because the stress drop of the foreshock is larger. In order to

compare events when the stress drops are significantly different, it is useful to use the minimum released strain energy, or available energy, to characterize the magnitude of the events.

Data Availability Statement

We used the GEONET F3-Solution (daily coordinate data of GNSS stations) published by the Geospatial Information Authority of Japan (https://www.gsi.go.jp/ENGLISH/geonet_english.html). The JIVSM was downloaded from https://www.jishin.go.jp/evaluation/seismic_hazard_map/lpshm/12_choshuki_dat/.

Acknowledgements

Generic Mapping Tools (GMT; Wessel et al. 2019) were used for figures and coordinate transformation. This study was supported by JSPS KAKENHI Grant Numbers JP19K04021and JP21K03729. This research was also supported by JSPS KAKENHI Grant Number JP21H05206 in Transformative Research Areas (A) “Science of Slow to Fast Earthquakes”

References

Agata, R., Barbot, S. D., Fujita, K., Hyodo, M., Iinuma, T., Nakata, R., et al. (2019). Rapid mantle flow with power-law creep explains deformation after the 2011 Tohoku mega-quake. *Nature Communications*, *10*(1), 1–4. https://doi.org/10.1038/s41467-019-08984-7

Aki, K., & Richards, P.G. (2002). Quantitative seismology.

Baba, T., Tanioka, Y., Cummins, P. R., & Uhira, K. (2002). The slip distribution of the 1946 Nankai earthquake estimated from tsunami inversion using a new plate model. *Physics of the Earth and Planetary Interiors*, *132*(1–3), 59–73. https://doi.org/10.1016/S0031-9201(02)00044-4

Baba, T., & Cummins, P. R. (2005). Contiguous rupture areas of two Nankai Trough earthquakes revealed by high-resolution tsunami waveform inversion. *Geophysical Research Letters*, *32*(8), 1–4. https://doi.org/10.1029/2004GL022320

Baranes, H., Woodruff, J. D., Loveless, J. P., & Hyodo, M. (2018). Interseismic coupling-based earthquake and tsunami scenarios for the Nankai Trough. *Geophysical Research Letters*, *45*(7), 2986–2994. https://doi.org/10.1002/2018GL077329

DeMets, C., Gordon, R. G., & Argus, D. F. (2010). Geologically current plate motions. *Geophysical Journal International*, *181*(1), 1–80. https://doi.org/10.1111/j.1365-246X.2009.04491.x

Fukuda, J., & Johnson, K. M. (2021). Bayesian inversion for a stress-driven model of afterslip and viscoelastic relaxation: method and application to postseismic deformation following the 2011 M_W 9.0 Tohoku-Oki Earthquake. *Journal of Geophysical Research: Solid Earth*, *126*(5), 1–35. https://doi.org/10.1029/2020JB021620

Graham, S. E., Loveless, J. P., & Meade, B. J. (2021). A Global set of subduction zone earthquake scenarios and recurrence intervals inferred from geodetically constrained block models of interseismic coupling distributions. *Geochemistry, Geophysics, Geosystems*, *22*(11), 1–30. https://doi.org/10.1029/2021gc009802

Hashimoto, C., Noda, A., Sagiya, T., & Matsu'Ura, M. (2009). Interplate seismogenic zones along the Kuril-Japan trench inferred from GPS data inversion. *Nature Geoscience*, *2*(2), 141–144. https://doi.org/10.1038/ngeo421

Hashimoto, C., Noda, A., & Matsu'ura, M. (2012). The Mw 9.0 northeast Japan earthquake: total rupture of a basement asperity. *Geophysical Journal International*, *189*(1), 1–5. https://doi.org/10.1111/j.1365-246X.2011.05368.x

Herman, M. W., Furlong, K. P., & Govers, R. (2018). The Accumulation of slip deficit in subduction zones in the absence of mechanical coupling: implications for the behavior of

megathrust earthquakes. *Journal of Geophysical Research: Solid Earth*, *123*(9), 8260–8278. https://doi.org/10.1029/2018JB016336

Herman, M. W., & Govers, R. (2020). Locating fully locked asperities along the south America subduction megathrust: A new physical interseismic inversion approach in a Bayesian framework. *Geochemistry, Geophysics, Geosystems*, *21*(8). https://doi.org/10.1029/2020GC009063

Hirose, H., & Obara, K. (2005). Repeating short- and long-term slow slip events with deep tremor activity around the Bungo channel region, southwest Japan. *Earth, Planets and Space*, *57*(10), 961–972. https://doi.org/10.1186/BF03351875

Hok, S., Fukuyama, E., & Hashimoto, C. (2011). Dynamic rupture scenarios of anticipated Nankai-Tonankai earthquakes, southwest Japan. *Journal of Geophysical Research*, *116*(B12), B12319. https://doi.org/10.1029/2011JB008492

Hori, T., Kato, N., Hirahara, K., Baba, T., & Kaneda, Y. (2004). A numerical simulation of earthquake cycles along the Nankai Trough in southwest Japan: Lateral variation in frictional property due to the slab geometry controls the nucleation position. *Earth and Planetary Science Letters*, *228*(3–4), 215–226. https://doi.org/10.1016/j.epsl.2004.09.033

Hori, T., Agata, R., Ichimura, T., Fujita, K., Yamaguchi, T., & Iinuma, T. (2021). High-fidelity elastic Green's functions for subduction zone models consistent with the global standard geodetic reference system. *Earth, Planets and Space*, *73*(1). https://doi.org/10.1186/s40623-021-01370-y

Ichinose, G. A., Thio, H. K., Somerville, P. G., Sato, T., & Ishii, T. (2003). Rupture process of the 1944 Tonankai earthquake (M_S 8.1) from the inversion of teleseismic and regional seismograms . *Journal of Geophysical Research: Solid Earth*, *108*(B10). https://doi.org/10.1029/2003jb002393

Iinuma, T., Hino, R., Uchida, N., Nakamura, W., Kido, M., Osada, Y., & Miura, S. (2016). Seafloor observations indicate spatial separation of coseismic and postseismic slips in the 2011 Tohoku earthquake. *Nature Communications*, *7*, 1–9. https://doi.org/10.1038/ncomms13506

Kato, A., Obara, K., Igarashi, T., Tsuruoka, H., Nakagawa, S., & Hirata, N. (2012). Propagation of slow slip leading up to the 2011 Mw 9.0 Tohoku-Oki earthquake. *Science*, *335*(6069), 705–708. https://doi.org/10.1126/science.1215141

Kimura, H., Tadokoro, K., & Ito, T. (2019). Interplate coupling distribution along the Nankai Trough in southwest Japan estimated from the block motion model based on onshore GNSS and seafloor GNSS/A observations. *Journal of Geophysical Research: Solid Earth*, *124*(6), 6140–6164. https://doi.org/10.1029/2018JB016159

Koketsu, K., Miyake, H., & Suzuki, H. (2012). Japan Integrated Velocity Structure Model version 1. *15th World Conference on Earthquake Engineering*, 1–4. Retrieved from http://www.iitk.ac.in/nicee/wcee/article/WCEE2012_1773.pdf

Li, S., Fukuda, J., & Oncken, O. (2020). Geodetic evidence of time-dependent viscoelastic interseismic deformation driven by megathrust locking in the southwest Japan subduction zone. *Geophysical Research Letters*, *47*(4), 1–10. https://doi.org/10.1029/2019GL085551

Lindsey, E. O., Mallick, R., Hubbard, J. A., Bradley, K. E., Almeida, R. V, Moore, J. D. P., et al. (2021). Slip rate deficit and earthquake potential on shallow megathrusts. *Nature Geoscience*. https://doi.org/10.1038/s41561-021-00736-x

Lorito, S., Romano, F., Atzori, S., Tong, X., Avallone, A., McCloskey, J., et al. (2011). Limited overlap between the seismic gap and coseismic slip of the great 2010 Chile earthquake. *Nature Geoscience*, *4*(3), 173–177. https://doi.org/10.1038/ngeo1073

Loveless, J. P., & Meade, B. J. (2011). Spatial correlation of interseismic coupling and coseismic rupture extent of the 2011 M W = 9.0 Tohoku-oki earthquake. *Geophysical Research Letters*, *38*(17), n/a-n/a. https://doi.org/10.1029/2011GL048561

Loveless, J. P., & Meade, B. J. (2015). Kinematic barrier constraints on the magnitudes of additional great earthquakes off the east coast of Japan. *Seismological Research Letters*, *86*(1), 202–209. https://doi.org/10.1785/0220140083

Maeda, T., Takemura, S., & Furumura, T. (2017). OpenSWPC: An open-source integrated parallel simulation code for modeling seismic wave propagation in 3D heterogeneous viscoelastic media 4. Seismology. *Earth, Planets and Space*, *69*(1). https://doi.org/10.1186/s40623-017-0687-2

Matsuzawa, T., Hirose, H., Shibazaki, B., & Obara, K. (2010). Modeling short- and long-term slow slip events in the seismic cycles of large subduction earthquakes. *Journal of Geophysical Research*, *115*(B12), B12301. https://doi.org/10.1029/2010JB007566

Melgar, D., LeVeque, R. J., Dreger, D. S., & Allen, R. M. (2016). Kinematic rupture scenarios and synthetic displacement data: An example application to the Cascadia subduction zone. *Journal of Geophysical Research: Solid Earth*, *121*(9), 6658–6674. https://doi.org/10.1002/2016JB013314

Miyazaki, S., McGuire, J. J., & Segall, P. (2011). Seismic and aseismic fault slip before and during the 2011 off the Pacific coast of Tohoku Earthquake. *Earth, Planets and Space*, *63*(7), 637–642. https://doi.org/10.5047/eps.2011.07.001

Murotani, S., Shimazaki, K., & Koketsu, K. (2015). Rupture process of the 1946 Nankai earthquake estimated using seismic waveforms and geodetic data. *Journal of Geophysical Research: Solid Earth*, *120*(8), 5677–5692. https://doi.org/10.1002/2014JB011676

Murphy, S., Di Toro, G., Romano, F., Scala, A., Lorito, S., Spagnuolo, E., et al. (2018). Tsunamigenic earthquake simulations using experimentally derived friction laws. *Earth and Planetary Science Letters*, *486*, 155–165. https://doi.org/10.1016/j.epsl.2018.01.011

Nikkhoo, M., & Walter, T. R. (2015). Triangular dislocation: an analytical, artefact-free solution. *Geophysical Journal International*, *201*(2), 1119–1141. https://doi.org/10.1093/gji/ggv035

Nishimura, T., Yokota, Y., Tadokoro, K., & Ochi, T. (2018). Strain partitioning and interplate coupling along the northern margin of the Philippine Sea plate, estimated from Global Navigation Satellite System and Global Positioning System-Acoustic data. *Geosphere*, *14*(2), 535–551. https://doi.org/10.1130/GES01529.1

Noda, A., Saito, T., & Fukuyama, E. (2018). Slip-deficit rate distribution along the Nankai Trough, southwest Japan, with elastic lithosphere and viscoelastic asthenosphere. *Journal of Geophysical Research: Solid Earth*, *123*(9), 8125–8142. https://doi.org/10.1029/2018JB015515

Noda, A., Saito, T., Fukuyama, E., & Urata, Y. (2021). Energy-based scenarios for great thrust-type earthquakes in the Nankai trough subduction zone, southwest Japan, using an interseismic slip-deficit model. *Journal of Geophysical Research: Solid Earth*. https://doi.org/10.1029/2020jb020417

Obara, K., & Kato, A. (2016). Connecting slow earthquakes to huge earthquakes. *Science*, *353*(6296), 253–257. https://doi.org/10.1126/science.aaf1512

Protti, M., González, V., Newman, A. V., Dixon, T. H., Schwartz, S. Y., Marshall, J. S., et al. (2014). Nicoya earthquake rupture anticipated by geodetic measurement of the locked plate interface. *Nature Geoscience*, *7*(2), 117–121. https://doi.org/10.1038/ngeo2038

Ruiz, S., Metois, M., Fuenzalida, A., Ruiz, J., Leyton, F., Grandin, R., et al. (2014). Intense foreshocks and a slow slip event preceded the 2014 Iquique Mw8.1 earthquake. *Science*, *1165*(6201), 1165–1169. https://doi.org/10.1126/science.1256074

Romanet, P., Sato, D. S. K., & Ando, R. (2020). Curvature, a mechanical link between the geometrical complexities of a fault: Application to bends, kinks and rough faults. *Geophysical Journal International*, *223*(1), 211–232. https://doi.org/10.1093/gji/ggaa308

Saito, T., & Noda, A. (2020). Strain energy released by earthquake faulting with random slip components. *Geophysical Journal International*, *220*(3), 2009–2020. https://doi.org/10.1093/gji/ggz561

Sagiya, T. (2004). A decade of GEONET: 1994–2003 —The continuous GPS observation in Japan and its impact on earthquake studies—, *Earth Planets Space*, 56, xxix–xli. https://doi.org/10.1186/BF03353077

637 Sagiya, T., & Thatcher, W. (1999). Coseismic slip resolution along a plate boundary megathrust:
638 The Nankai Trough, southwest Japan. *Journal of Geophysical Research: Solid Earth*,
639 *104*(B1), 1111–1129. https://doi.org/10.1029/98JB02644

640 Sasajima, R., Shibazaki, B., Iwamori, H., Nishimura, T., & Nakai, Y. (2019). Mechanism of
641 subsidence of the Northeast Japan forearc during the late period of a gigantic earthquake
642 cycle. *Scientific Reports*, *9*(1), 1–13. https://doi.org/10.1038/s41598-019-42169-y

643 Savage, J. C. (1983). A dislocation model of strain accumulation and release at a subduction
644 zone. *Journal of Geophysical Research: Solid Earth*, *88*(B6), 4984–4996.
645 https://doi.org/10.1029/JB088iB06p04984

646 Segall, P., & Bradley, A. M. (2012). Slow-slip evolves into megathrust earthquakes in 2D
647 numerical simulations. *Geophysical Research Letters*, *39*(17), 2–6.
648 https://doi.org/10.1029/2012GL052811

649 Sherrill, E. M., & Johnson, K. M. (2021). New Insights into the slip budget at Nankai: An
650 iterative approach to estimate coseismic slip and afterslip. *Journal of Geophysical*
651 *Research: Solid Earth*, *126*(2), 1–23. https://doi.org/10.1029/2020JB020833

652 Takagi, R., Uchida, N., & Obara, K. (2019). Along-strike variation and migration of long-term
653 slow slip events in the western Nankai Subduction zone, Japan. *Journal of Geophysical*
654 *Research: Solid Earth*, *124*(4), 3853–3880. https://doi.org/10.1029/2018JB016738

655 Takemura, S., Okuwaki, R., Kubota, T., Shiomi, K., Kimura, T., & Noda, A. (2020). Centroid
656 moment tensor inversions of offshore earthquakes using a three-dimensional velocity
657 structure model: Slip distributions on the plate boundary along the Nankai Trough.
658 *Geophysical Journal International*, *222*(2), 1109–1125. https://doi.org/10.1093/gji/ggaa238

659 Tanioka, Y., & Satake, K. (2001). Coseismic slip distribution of the 1946 Nankai earthquake and
660 aseismic slips caused by the earthquake. *Earth, Planets and Space*, *53*(4), 235–241.
661 https://doi.org/10.1186/BF03352380

662 Wang, K., & Dixon, T. (2004). "Coupling" Semantics and science in earthquake research. *Eos,*
663 *Transactions American Geophysical Union*, *85*(18), 180.
664 https://doi.org/10.1029/2004EO180005

665 Watanabe, S. I., Bock, Y., Melgar, D., & Tadokoro, K. (2018). Tsunami Scenarios Based on
666 Interseismic Models Along the Nankai Trough, Japan, From Seafloor and Onshore
667 Geodesy. *Journal of Geophysical Research: Solid Earth*, *123*(3), 2448–2461.
668 https://doi.org/10.1002/2017JB014799

669 Wessel, P., Luis, J. F., Uieda, L., Scharroo, R., Wobbe, F., Smith, W. H. F., & Tian, D. (2019).
670 The Generic Mapping Tools version 6. *Geochemistry, Geophysics, Geosystems*, *20*(11),
671 5556–5564. https://doi.org/10.1029/2019GC008515

672 Yang, H., Yao, S., He, B., Newman, A. V., & Weng, H. (2019). Deriving rupture scenarios from
673 interseismic locking distributions along the subduction megathrust. *Journal of Geophysical*
674 *Research: Solid Earth*, *124*(10), 10376–10392. https://doi.org/10.1029/2019JB017541

675 Yokota, Y., Ishikawa, T., Watanabe, S., Tashiro, T., & Asada, A. (2016). Seafloor geodetic
676 constraints on interplate coupling of the Nankai Trough megathrust zone. *Nature*,
677 *534*(7607), 374–377. https://doi.org/10.1038/nature17632

678